Imperial College of Science, Technology and Medicine
University of London

Measurements of local heat transfer coefficient and film cooling effectiveness in turbine blade tip geometries

Jae Hyun Yoon, Dr. R. F. Martinez-Botas

September 2001

Thermofluids Section
Department of Mechanical Engineering

REPORT DOCUMENTATION PAGE

Form Approved OMB No. 0704-0188

1. REPORT DATE *(DD-MM-YYYY)*	2. REPORT TYPE	3. DATES COVERED *(From – To)*
2001	Final Report	8/18/99 - 18-Feb-00

4. TITLE AND SUBTITLE

Measurements of local heat transfer coefficient and film cooling effectiveness in turbine cooled tip geometries

5a. CONTRACT NUMBER
F61775-99-WE095

5b. GRANT NUMBER

5c. PROGRAM ELEMENT NUMBER

6. AUTHOR(S)

Professor Ricardo Fernando Martinez Botas Mateo

5d. PROJECT NUMBER

5d. TASK NUMBER

5e. WORK UNIT NUMBER

7. PERFORMING ORGANIZATION NAME(S) AND ADDRESS(ES)

Imperial College of Science, Technology and Medicine
Exhibition Rd.
London SW7 2BX
United Kingdom

8. PERFORMING ORGANIZATION REPORT NUMBER

N/A

9. SPONSORING/MONITORING AGENCY NAME(S) AND ADDRESS(ES)

EOARD
PSC 802 BOX 14
FPO 09499-0200

10. SPONSOR/MONITOR'S ACRONYM(S)

11. SPONSOR/MONITOR'S REPORT NUMBER(S)
SPC 99-4095

12. DISTRIBUTION/AVAILABILITY STATEMENT

Approved for public release; distribution is unlimited.

13. SUPPLEMENTARY NOTES

14. ABSTRACT

This report results from a contract tasking Imperial College of Science, Technology and Medicine as follows: The project will involve the quantification of the flow and surface characteristics of turbine blade tip cooling geometry with velocity and turbulence distributions relevant to the gas turbine designer. The experimental program will provide measurements of the film cooling adiabatic effectiveness and heat transfer coefficient in a simulated blade tip, with injection from the pressure surface side near the tip. The program will be progressive and interactive, starting with a single row of film cooling holes with injection from the pressure surface side near the tip, moving towards other representative injection configurations: slot injection on the tip surface and groove-tip geometry. The project will supply validation data for the 3D Navier-Stokes solver Glenn-HT, currently used by NASA, and it will also provide insight into the performance of advanced cooling geometry configurations.

The experiments will make use of liquid crystal thermography to obtain the heat transfer data. The data acquisition method corresponds to the steady-state technique with the use of wide band liquid crystals. It requires a reduced number of experiments when compared with narrow band crystals and thermocouples, and provides a high degree of spatial resolution and reduced uncertainty level. It will be accompanied by data from small-diameter thermocouples, hot wires and pressure transducers.

15. SUBJECT TERMS
EOARD, Gas Turbines, Turbine Blade Cooling

16. SECURITY CLASSIFICATION OF:			17. LIMITATION OF ABSTRACT	18, NUMBER OF PAGES	19a. NAME OF RESPONSIBLE PERSON
a. REPORT	b. ABSTRACT	c. THIS PAGE			Charbel N. Raffoul
UNCLAS	UNCLAS	UNCLAS	UL	56	19b. TELEPHONE NUMBER *(Include area code)* +44 (0)20 7514 4299

Abstract

An experimental investigation of the local film cooling effectiveness and heat transfer coefficient downstream of a row of elongated holes into a simulated axial turbine blade tip is presented. Film cooling is needed to protect the turbine blade tip region from high heat transfer rates, especially when convection internal cooling is insufficient to keep the blade metal temperature distribution within the limits required by the blade life. Accurate heat transfer predictions in this region of the blade are particularly difficult given the three dimensionality of the flow and the narrow passage typical of turbine blades. It is thus important to provide experimental data to validate the numerical approach.

The experimental technique used is the wide band liquid crystal thermography. This technique is capable of achieving full coverage of the measurement of the surface temperature, from which the effectiveness and heat transfer coefficient measurements can be found with typical uncertainties of 4% and 8% respectively.

The effect of Reynolds number and blowing ratio are examined for an injection on the blade tip itself close to the pressure surface corner.

Film cooling effectiveness increased with increase blowing ratio for all the cases tested ($M = 0.1 \sim 1.2$), thus no optimum blowing ratio can be proposed. The corresponding results for heat transfer coefficient result show an argumentation of this value with an increased blowing ratio due to an increased interaction of jet flow with the cross flow.

Limited computational results are available for comparison but a comparison with a predicted on similar geometry found a significant disagreement for the prediction of heat transfer coefficient, while the prediction of adiabatic wall effectiveness was good except very close to injection hole.

Contents

List of Tables

List of Figures

Nomenclature

A	constant in Kings Law
ABS	Acrylonitrile butadiene styrene polymer
b	thickness of test plate
B	the colour blue
B	constant in Kings law
C	mass fration
CCD	charge-couple device
CJD	cold junction compensation for thermocouples
C_p	specific heat capacity at constant pressure (J/kgK)
D	hole diameter
DR	density ratio (ρ_2/ρ_∞)
$erfc$	error function
F	correction factor
g	gravitational acceleration $(9.81m/s^2)$
G	gain used in the signal conditioner for hot-wire anemometry
G	the colour blue
H	hue value of colour
h	heat transfer coefficient (W/m^2K)
h_0	heat transfer coefficient in the absence of film cooling (W/m^2K)
$h_{b\infty}$	heat transfer coefficient in the absence of film cooling (W/m^2K)
HSI	colour space hue, saturation and intensity
i	current
I	intensity
k	thermal conductivity (W/mK)
L	hole length
L	thickness of individual layer in constant heat flux composite
M	blowing ratio $(\rho_2 U_2/\rho_\infty U_\infty)$
Ma	Mach Number.

n	number of data points
Nu	Nusselt number (hx/k)
O	offset used in signal conditioner for hot-wire anemometry
P	pitch
P	hut value of each pixel
$P.S$	pressure surface
PET	polyethylene terephthalate (polyester)
Pr	Prandtl number (μ/Γ)
PVC	polyvinyl chloride
Q	volumetric flow rate (l/min)
$q^{"}$	wall heat flux(W/m^2)
$q^{"}_{bc}$	heat loss per unit area due to conduction from black of heater
$q^{"}_{g}$	average heat flux generated in the heater
$q^{"}_{r}$	heat loss per unit area due to thermal radiation
R	the colour red
R	correlation of curve fit
Re_D	freestream Reynolds number based on hole diameter $(\rho UD/\mu)_\infty$
Re_x	freestream Reynolds number based on x $(\rho Ux/\mu)_\infty$
RGB	colour space red, green and blue
rms	root mean squared
R_t	summation of thermal resistance
S	saturation value of colour
$S.S$	suction surface
Sh	Sherwood number $(hx/c\tau)$
St	Stanton number $(q^{"}/\rho C_p U_\infty(T_{w0} - T_\infty))$
t	time (t)
T	temperature (K)
Tu	turbulence intensity
U	velocity (m/s)
v	measured voltage drop across heater plate $(volts)$
VR	coolant-to-freestream velocity ratio
x	coordinate: streamwise(axial) direction
y	coordinate: streamwise(height-wise) direction from the wall
z	coordinate: lateral direction from the centre of the hole

Greek Symbols

α	streamwise injection angle measure from the test wall
β	lateral orientaion
δ	boundary layer thickness (99% of the freestream velocity)
δ^*	displacement thickness
δ_i	momentum thickness
Δ	thermal boundary layer thickness
ΔT_{lw}	temperature loss in thermocouple lead wire (K)
ε	emissivity of liquid crystal
Γ	thermal diffusion coefficient (k/C_p)
η	film cooling effectiveness $(T_{aw} - T_\infty)/(T_2 - T_\infty)$
μ	dynamic viscosity (Ns/m^2)
ν	kinematic viscosity (m^2/s)
ρ	density (kg/m^3)
σ	stefan-Boltzmann constant $(5.67 \times 10^{-8} W/m^2K^4)$
Σ	summation
ξ	unheated starting length

Subscripts

∞	freestream
0	in the absence of film cooling
2	coolant
ATP	atmospheric temperature and pressure
aw	adiabatic wall
fs	freestream
ini	inital
TLC	thermographic liquid crystal
w	wall

Overbar

$\hat{}$	laterally-averaged over one pitch mean value

Chapter 1

Introduction

1.1 Introduction

The desire for the higher efficiency and specific thrust in gas turbine system has lead to an increase in attention devoted to the heat transfer aspects throughout the gas turbine components. An increase in turbine entry temperature is required to achieve this objective, however this means gas turbine components are exposed to adverse thermal environments where turbine blade material temperature exceeds its limits, and have to be protected from hot gases with effective cooling systems. Turbine inlet temperature has almost doubled over a past 25 years, a direct result of this has been an improvement in blade cooling methods and the development of high temperature resistant materials. Detailed attention in turbine blade cooling technology of the gas turbine engine is required for further improvements in engine performance and durability.

The cooling air used is taken from the engine compressor later stages; this extraction of the high-pressure air from engine compressor stage has a negative effect on overall cycle thermal efficiency. The minimization of cooling air used is another important motivation for the development of improved prediction method for convection heat transfer in turbine blade.

One of the most problematic cooling areas in gas turbine engines is the blade tip region, especially near trailing edge where it is very difficult cool it sufficiently. In all configurations with unshrouded tips, a clearance gap exist between the turbine blade and outer shroud. This gap exists even in turbine with advanced clearance control mechanisms, Hennecke (1984).

The pressure difference between the suction and pressure side of the turbine blade drives a sink like flow through the clearance gap between the blade tip and shroud. This flow is generally known as tip leakage flow. It is composed of both mainstream fluid from the hot gas path regions near the blade tip and cooler fluid from the blade pressure surface near the tip. This combination of high gas temperatures entering the clearance gap induces high convective heat transfer coefficients on the blade tip surface. The resultant thermal loading can be significant and detrimental to the turbine blade tip durability leading to early failures. A widening of the clearance gap due to significant oxidation and material weight loss can rapidly occur thus increasing in leakage flow loss.

A typical clearance gap flow is illustrated in Fig. 1.1, where the arrows represent the motion of the gas close to the tip of the blade. The tip width from pressure to suction side varies along the blade-chord. The flow path length can be up to 20 times the gap height over the widest part at the turbine blade tip. It is thus possible to derive an experiment representation of this wide region in a simplified wind tunnel experiment.

Film cooling can be provided in a variety of different configurations:

- by means of a series of holes located on the tip itself - providing a protection not dissimilar to film cooling in the main blade (Fig. 1.2).
- by injecting on the blade pressure surface thus allowing the leakage flow to take the cold air over the tip at the blade, thus providing protection in the critical portion of the pressure surface/tip corner (Fig. 1.3).
- by introducing cavities on the blade tip itself and providing coolant air to this cavities - this is also know as squealer tip configuration (Fig. 1.4).

The current report will only over the first of these cooling configurations. It is intended to extend this work to the other arrangements as part of the current experimental program.

The clearance gap is normally in the order of one percent of the blade height and given such a narrow flow inlet gap and relatively long streamwise passage, the relative motion between the two parallel walls of the gap might have a significant effect on the magnitude of convection of the blade tip. Mayle et al. (1982) experimentally showed that the clearance gap leakage flow is mainly caused by the pressure loading distribution existing between the pressure side and the suction side of the turbine blade. They also showed that the relative motion between tip and shroud does not effect in calculation of the heat transfer coefficient on the tip. This independence has been also established in an

experimental investigation of Chyu et al. (1987) in a wide range of operating conditions with a rectangular cavity geometry. The above conclusion support blade tip heat transfer coefficient can be determined without a moving wall.

1.2 Aim of Research

The current study aims to provide a comprehensive set of experimental measurement of the film cooling effectiveness and heat transfer coefficients on a wide range of operating conditions in the turbine blade tip region in order to improve understanding of the fluid/heat transfer and improve convective heat transfer methods by means of validation against NASA Glen-HT (3-Dimensional Reynolds-averaged Navier-Stokes solver).

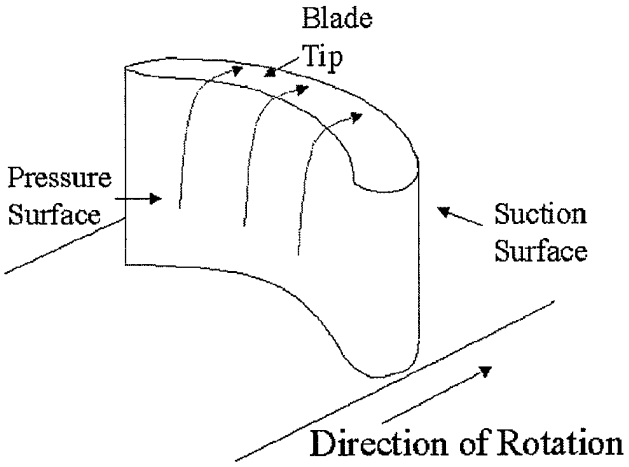

Figure 1.1: Clearance tip leakage flow

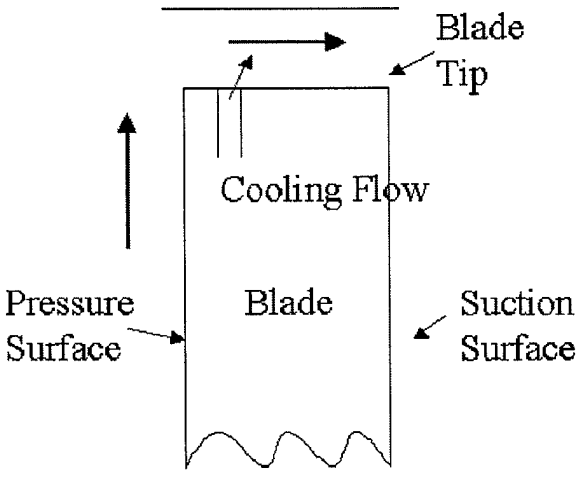

Figure 1.2: Tip Clearance Injection

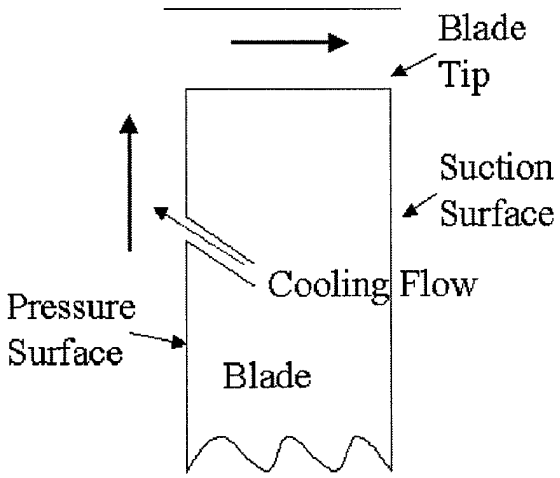

Figure 1.3: Pressure Side Injection

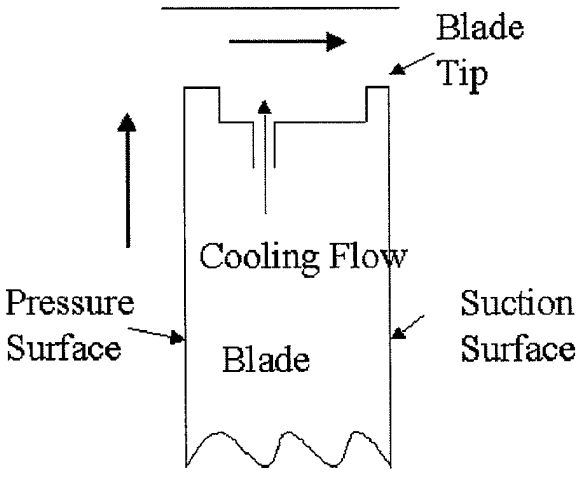

Figure 1.4: Grooved (Squealer) Tip Injection

Chapter 2

Literature Survey

2.1 Theory of Heat Transfer in Film Cooled Surface

The heat transfer coefficient and film cooling effectiveness are used to quantify measurement of the test surface convection and evaluation of the performance of the film cooling, Goldstein (1971). These two parameters can be further combined give an overall performance measurement know as the net heat flux reduction parameter. These are defined in subsequent paragraphs.

In this experiment, film heating rather than film cooling is employed for reasons of convenience in designing the test rig. In small temperature differences, the flow can be considered as a constant property and the dimensionless temperature distribution in the boundary layer will be independent of whether the secondary gas is hotter or colder than the main stream. This is an important assumption in the calculation of the heat transfer coefficient where a heated wall is used.

2.1.1 Heat Transfer Coefficient

The heat transfer coefficient should be independent of the temperature difference for a constant property flow. The heat transfer coefficient is commonly defined as:

$$h = \frac{q''}{(T_w - T_{dat})} \tag{2.1}$$

where h is the local heat transfer coefficient (W/m^2K), q'' is the wall heat flux (W/m^2), T_w is the local wall temperature and T_{dat} is the datum temperature. In a perfectly insulated surface the heat flux would be zero and the resulting surface temperature is the adiabatic wall temperature T_{aw}(K). In this case the adiabatic wall temperature could be replaced as the datum temperature.

$$h = \frac{q''}{(T_w - T_{aw})} \tag{2.2}$$

with this definition of datum temperature, the heat transfer coefficient becomes independent of the temperature difference for a constant property flow. The adiabatic wall temperature represents the limiting value of the wall temperature that can be obtained without an internal wall cooling.

The heat transfer coefficient can also be defined as Eqn. 2.3 when the injection and freestream are at the same temperature, Eriksen (1971).

$$h = \frac{q''}{(T_w - T_\infty)} \tag{2.3}$$

where h are the local heat transfer coefficient and T_∞ is the freestream temperature for a subsonic flow. This definition is used to calculate the heat transfer coefficient with unheated injection with a given heat flux input.

The objective of film cooling is to achieve low heat transfer from the surrounding hot mainstream to the turbine blades, and large effectiveness on the blade surface to provide protection from convection heat transfer to the surface from the high temperature mainstream flow.

2.1.2 Film Cooling Effectiveness

In film cooling, the reference temperature (adiabatic wall temperature) is at some general unknown level that depends on the supply temperature of two interacting streams and the degree of mixing that has occurred before they arrive at the various locations of the test surface.

The adiabatic-wall temperature (T_{aw}) is usually presented in dimensionless form as the film cooling effectiveness (η) defined in Eqn. 2.4 for a low speed and a constant property flow.

$$\eta = \frac{(T_{aw} - T_{\infty})}{(T_2 - T_{\infty})} \tag{2.4}$$

where T_2 and T_{∞} are the respective temperatures of the coolant and the mainstream. The mainstream temperature is replaced by the recovery temperature in high-speed flows. This effectiveness represents the efficiency of a cooling film, a value of unity is achieved when the adiabatic wall temperature is the same as the coolant temperature thus achieving maximum protection. A value of zero is achieved when the adiabatic wall temperature is same as the free stream temperature, thus the wall is totally unprotected by the film cooling flow issuing from the holes.

2.2 Measurement Technique

Various experimental methods have been developed by researchers to determine the film cooling effectiveness and the heat transfer coefficient. The experimental method used in this study is based on steady-state heat transfer technique. This method can obtain both heat transfer coefficient and effectiveness values in two experiment by either employing a constant heat flux surface or a nominally adiabatic surface. An alternative is the mass transfer method, it uses the analogy between heat and mass transfer characteristic and it avoids the difficulties in achieving a truly an adiabatic test surface as in the steady-state heat transfer method, Rastogi (1972) and Ammari (1989). The final method is the transient heat transfer method, where in a single transient experiment it is possible to obtain both h and η by solving the one dimensional heat conduction equation. A summary of these techniques are given in the following sections.

2.2.1 Heat Transfer Method

The heat transfer method (either transient or steady-state) is the most widely used method to determine the heat transfer coefficient and effectiveness. In the past, a large number of thermocouples was used to obtain temperature of the test surface, but resolution of surface temperature was limited to the number of thermocouples. Thin layer of cholesteric liquid crystals over the heated surface are used to overcome this difficulties. The crystals produce unique color signal in repose to different temperatures. This thermal visualization determines the surface temperature and it is used to calculate the local heat transfer

coefficient and the film cooling effectiveness, in different walls depending on the technique chosen.

Steady State Technique

Typical steady state experiments involve an electrically heated constant heat flux surface with a cold mainstream, and heated secondary injection thus giving film heating; the reverse would provide film cooling (hot main stream and cold secondary injection). It is often more economical and convenient to design a steady state heat transfer experiment with film cooling. From Eqn. 2.2,

$$h = \frac{q''}{(T_w - T_{aw})} \tag{2.5}$$

the heat flux, q'', and both the wall temperature, T_w, and adiabatic wall temperature T_{aw} are required to obtain heat transfer coefficient.

A constant heat flux at the surface can be provided with a graphite impregnated paper or thin stainless steel foil. The uniform resistance of the membrane is important in providing the constant heat flux and the thin metal foils are more suitable in this case, otherwise power distribution is difficult to calculate. Electrical power supply measurement for a constant heat flux surface are need to obtain the heat flux.

In the case of an unheated injection, where the injection flow temperature is equal to mainstream temperature, the mainstream recovery temperature is used as the adiabatic wall temperature. For the heated injection, the adiabatic wall temperature has to be measured on an adiabatic test surface (i.e $q'' = 0$) in a separate experiment with unheated wall. The unheated wall with a heated injection experiment provide experimental data for the film cooling effectiveness calculation.

Transient Technique

The transient technique usually involves an initial temperature difference between the flow and the model. Metzger and Larson (1986) exposed their test models to preheated mainstream or Martinez-Botas et al. (1995) exposed preheated models to an ambient temperature. If the model has a low thermal conductivity and the measurements are made in a short time, the heat transfer can be approximated to a one dimensional problem. This assumes the thermal penetration depth is negligible compared to the wall thickness of the

model. With this assumptions, the heat transfer coefficient can be calculated from the 1-D unsteady heat transfer, Eqn. 2.6, giving the well known solution:

$$\frac{T_{wall} - T_{ini}}{T_{gas} - T_{ini}} = 1 - e^{\frac{h^2 t}{m}} erfc(\frac{h\sqrt{t}}{\sqrt{m}}) \tag{2.6}$$

where T is temperature, h is heat transfer coefficient, m is the product of $\rho\kappa C_p$ and t is time.

The transient technique inheritably contains a relatively larger error than steady state technique due to difficulty in determining the elapsed time and the validity of the assumption of a semi-infinite solid. Vedula and Metzger (1991) reported uncertainties of $\pm 8\%$ in h and $\pm 12\%$ in η for transient technique measurements and Ekkad et al. (1997) similarly shows uncertainties level of $\pm 6.5\%$ for h and $\pm 8.5\%$ for η measurements.

2.2.2 Mass Transfer Method

The accurate measurement of local heat transfer in the heat transfer methods (steady or transient) is difficult due an unavoidable error produced by heat conduction within the surface. The alternative method is utilising the mass transfer analogue technique which uses the sublimation of naphthalene. The test surface consists of a removable naphthalene, the local mass transfer coefficients can be found from the local mass fractions of sublimed naphthalene surface according to,

$$\eta = \frac{(C_w - C_\infty)}{(C_2 - C_\infty)} \tag{2.7}$$

where C_w represents the local wall mass fraction, C_∞ is the mass fraction of the freestream, and C_2 the coolant mass fraction. The weight of the naphthalene on the test surface before and after exposure to the air streams determines the mass transfer rate. The local thickness of the layer is measured with an accurate mechanical depth gauge. This method is valid when Schmidt number for mass transfer is equal to the Prandtl number to satisfy the analogy of the heat transfer situation.

2.3 Previous studies on blade tip cooling

The pressure difference between the suction and pressure sides of the blade induces flow through the clearance gap. The blade tip leakage flow has been subjected to a detailed

investigation, given that the blade tip losses represent a major efficiency penalty in a turbine blade and this region is prone to early failure due to insufficient cooling.

Lakshminaryana (1970) developed an analytical expression for the decrease in stage efficiency due to tip clearance loss and compared it existing experimental data. He suggested an optimum clearance where the losses and flow departures are minimal. The methodology for predicting and minimizing tip leakage flows was also developed with help of the water table cascade rig by Booth et al.(1982) and showed that the tip leakage flow is predominantly an invisid phenomena. It treated normal velocity component of the blade tip leakage flow in terms of discharge coefficient, simple discharge experiment with a cascade model were adopted for improvements in tip leakage configurations.

Bindon (1986) measured tip clearance flow for the leading to trailing edge of a linear turbine cascade model and identified and quantified loss mechanisms with the clearance flow. Simple flow visualization techniques showed details of the flow structure in and around the tip clearance region. Mixing, internal shear flow, and secondary flows were identified and discussed. Sjolander and Cao (1995) conducted similar experimental measurement in a single idealized, large scale tip gap model with this larger scale it was possible to obtain more detailed measurement inside the clearance gap. In both cases, the sharp corner at the entrance of the gap induced a separation bubble formation in the early portion of the clearance gap.

In more recent years, attention has focused on the heat transfer aspect of the tip leakage flows. Heat transfer rates on the tip of the blade have been determined in various studies and the result show that they are some of the highest of all turbine components. An experimental and numerical investigation of local convective heat transfer at the tip region with different tip geometry were conducted by various researchers. Metzger and Rued (1989) investigated influence of tip leakage flow on heat transfer and flow development along the pressure side of the turbine blade. The clearance flow field measurements were conducted with a laser-doppler anemometer to aid interpretation of the heat transfer results and found that very high velocities and accelerations are generated very near the clearance gap. Chyu et al. (1989) used the naphthalene sublimation technique to determine detailed heat transfer characteristic. The heat transfer coefficient measurement was strongly influenced by geometrical effect of the cavity, is similar to the one shown in Fig. 1.4.

Malye and Metzger (1982) established that the relative motion between flat blade tip and stationary shroud have a negligible effect on convection tip heat transfer coefficient. Chyu et al. (1987) introduced a grooved turbine blade tip geometry to decrease the pressure

difference between the suction and the pressure side of the blade and therefore reducing the clearance gap flow. The effect of shroud motion are confined to a thin layer adjacent to the shroud in both cases. The cavity region flow patterns, mean velocity profiles and heat transfer coefficient are virtually independent of relative motion.

Most of the published work concentrate on clearance gap flows but not on the tip cooling system associated with a cooled tip. There are only a limited published experimental and computational data in film cooling injection for the simulated turbine blade tips. Kim and Metzger (1995) and Kim et al (1995) measured heat transfer and film effectiveness for various combinations of clearance gap heights, flow Reynolds number and the blowing ratio with different injection geometries using a transient thermal liquid crystal technique. The data shows strong dependency of film cooling performance on the choice of the coolant supply hole shapes and injection locations for a given tip geometry.

In terms of numerical work, Chen et al. (1993) used a two-dimensional Navier-Stokes equation model to simulate the effect of tip flow Reynolds number for flat and squealer types of blade tips, these were compared with experimental measurement The results showed that secondary injection into the tip gap leads to a reduction of the total mass flow entering the gap.

However, the two-dimensional simulation impose severe limitations on the range of geometries. Ameri and Ridgby (1999) used a three-dimensional Reynolds-averaged Navier-stokes solver to predict the rate of tip heat transfer and film cooling effectiveness on a simulated blade tip and provided numerical flow visualization of the cooling fluid distribution on the clearance gap. The heat transfer prediction grid resolution dependent and required high grid resolutions.

Chapter 3

Experimental Set Up

3.1 Introduction

This chapter present a detailed description of the experimental set up, measurement techniques and test procedure. Details of data reduction techniques and uncertainty estimates are also discussed. The measurements of film cooling effectiveness and heat transfer coefficient with a steady state heat transfer method is based on wide band liquid crystals thermography. Experiments were conducted for a test matrix shown in the Table 3.1 and Table 3.2. A colour contour plot of both heat transfer coefficient and film cooling effectiveness over the test surface downstream of injection are used to discuss film cooling characteristics. The laterally-averaged values can be derived from these colour maps.

3.2 Test Facility

The experimental setup focuses on a small part of the whole tip leakage problems. It simulates the pressure side corner as the blade tip where the tip leakage enters the tip clearance gap. A diagram of the experimental apparatus used in the present study is shown in Fig. 3.1.

Wind Tunnel

An open-circuit wind tunnel is used in the current investigation to provide primary air supply, it consist of blower followed by a high aspect ratio contraction. The air is turned though 90° bend and feds into a narrow passage simulating the tip cooling injection.

The Injection System and Plenum chamber

The secondary flow circuit is shown in Fig. 3.2. The air injectant or secondary air is supplied from the filtered laboratory compressor air. The injectant flow rate was controlled by a needle valve and the volumetric flow rate was measured by a rotameter. Flow then passes through an inline pipe heater, followed by a plenum chamber that supplies the injection plate. A flow straightener is inserted in the upstream of the rotameter to achieve uniform flow. A small or a large flow capacity rotameter was used to obtain an accurate measurement of the volumetric flow rate to cover a wide range of secondary flow rate. The pressure gage is required to measure back pressure which is used to calculate true volumetric flow rate.

For a heat injection experiment, a 1890W in-line heater, which was controlled by a variac, was adjusted to provide a heated jet at $40°C \pm 0.1°C$. The temperature difference between free stream and jet was under $20°C$, and this small difference is important to satisfy the constant property flow assumption previously mentioned. The jet temperature is measured with a thermocouple at the two diameters into the injection plate.

A narrow plenum chamber with three fine gauze screens was connected to the outlet of an inline pipe heater. The plenum chamber was designed to smoothing out any velocity non-uniformity. The uniformity test showed a maximum non-uniformity of $\pm 5\%$ in the distribution across the injection holes.

Test Plates

A 50 mm by 360 mm injection plate is shown in Fig. 3.3. The test plate is manufactured and machined from Polyster Polyethlene Threphthalate (PET) which has a high thermal conductivity and less brittle hence easier to machine than Perspex. It is designed to be interchangeable with other plates with different cooling hole geometries for the further investigation of geometrical effects of the film cooling.

The test plate has one row of five elongated holes with 90° inclined to the test surface in the streamwise direction. The holes were arranged in a way that the central hole lied on the centreline of the test plate where the liquid crystals are painted on. The trailing edge of the holes was 24mm away from the downstream edge of the test plate. This is equivalent to 1.5 hole diameter distance. This space is compromised by the space required for the plenum chambers underneath the injection plate.

The purpose of neighboring holes was to ensure the fluid dynamical environment which simulates the jet interaction present in three dimensional film cooling situations. The main area of interest in the measurement area is in the vicinity of the central hole and the hole adjacent to the central hole in order to remove the side-wall effect of the wind tunnel.

Constant Heat Flux Surface

A 360mm wide by 1000mm long composite test plate was designed to produce a constant heat flux with a minimum lateral conduction across the plate. The constant heat composite consists of 0.2mm thick stainless steel sheet, it is heated with 18 inconnel strips which covers entire width of the test surface. The heating element, each with 54mm width are connected to the electrical power supply by a series of 3m thick copper bus bars on each end of the test plates (see Fig. 3.4).

Rastogi (1972) used electrical current directly to the stainless steel test surface but this technique require a large current and prone to suffer from non-uniform resistance which could lead to non uniform heat flux distribution. Ericksen (1971) used serpentine Inconel strips without silicon impregnated sheet. In the current experiment, 0.2mm thick silicon impregnated sheet was placed in between the stainless steel sheet and the Inconel heater strip. This silicon sheet provided electrical insulation and promoted heat conduction to the test surface so as to improve the uniformity of heat flux distribution.

A gap of 1mm between the adjacent heater strips is required for electrical insulation, a typical gap size between the adjacent metal stipes was 1mm by Sen at la. (1996).

The T-type copper-constantan thermocouples with PVC casing and a nominal size of 0.43×0.71mm were connected in the composite test plate. These thermocouples were installed to 10 different pre-determined places on the stainless steel sheet. These thermocouples are required for calibration of liquid crystals.

A single phase transformer with two 25 volts r.m.s secondary winding operating at 35

amperes was made to power the heating elements. The uniformity resistance of Inconel strips was checked with measuring voltage across a given distance before the layer of stainless sheet was mounted. Further assessment of uniformity of heat flux was carried out with the liquid crystal coating. At a given electrical setting and operating conditions, standard divination of temperature measured was 0.2 degree on the entire test plate.

3.3 Liquid Crystal Thermography

3.3.1 Test Surface

The microencapsulated liquid crystal used in the current study were supplied by Thermax with a bandwidth of 10°C. The upper surface of stainless steel sheet was first coated with black paint with an airbrush. The microencapsulated liquid crystal was then airbrushed over the black paint. The experimental set up is shielded from room light and room air currents using anti-flammable tick black curtain draped over the of a support structure. The test plate thus receives only incident light emitted from the arc light and eliminates variations in illumination. The shield is also required to protect the liquid crystal surface form UV radiation damages. An Hoya polarising filter was installed onto the camera lens to minimize reflections of the Perspex roof of the working section.

3.3.2 Application of Thermographic Liquid Crystals

The reflected light from liquid crystals is dependent on the spectral intensity of the incident light and contains a peak whose wavelength depends on the given temperature. RGB(red, green, and blue) is commonly used to define colour. The data to define RGB colour format requires three times that of grey scale, the relationship between the combination of RGB format and temperature are not simple since RGB signal is dependent on the local illumination strength.

Colour CCD cameras generally use three individual filters to determine R, G, and B components of light. RGB components can then be converted into a variety of different representations for colour. The more appropriate format is to use the HSI format (hue, saturation and intensity). HSI format is a simple and monotonic format of the wavelength of the colour signal. Camci at al. (1992) suggests that hue alone can be used to represent the peak wavelength of temperature of the liquid crystal. The hue, saturation and

intensity are defined in Eqn. 3.1, Eqn. 3.2 and Eqn. 3.3. Hue describes colour, saturation describes the degree of which a pure colour is diluted with white, and intensity is a colour-neutral attribute that describes brightness or darkness. Hue value is independent of the local illumination strength and have a direct relationship between the local temperature and the locally measured hue value.

$$Hue = \frac{1}{360}[90 - \arctan\{\frac{F}{\sqrt{3}}\}], \tag{3.1}$$

where $F = \frac{2R-G-B}{G-B}$ for G≠B, F=R for G=B

$$Saturation = 1 - \frac{min(R,G,B)}{I} \tag{3.2}$$

$$Intensity = \frac{R+G+B}{3} \tag{3.3}$$

3.4 Imaging System

3.4.1 Working Section

The test section has a cross-sectional area of 165 x 110 mm^2 and is 800mm long and simulates a turbine blade tip clearance gap of 40mm, as shown in Fig. 3.6 and Fig. 3.7. The perspex roof allows optical access for the imaging system and side windows provide good optical access, as well as thermal insulation. The perspex is used to minimize conduction loss.

3.4.2 Data Acquisition and Processing

Images were captured by a JVC colour CCD camera (TK-885E) which was controlled by a 24-bit frame grabber installed in a Pentium 3 computer and positioned directly over test plate. The images are captured and stored as a three-dimensional matrix of red, green and blue (RGB) values. A code was written to control the capture rate (25 frames per second), and the sequence of images was stored on hard disk for post-processing. Once

images were stored for the each test case, image processing was then conducted. The RGB images on each were first converted to hue, saturation and intensity (HSI) colour space using a commercial software, and then split into hue, saturation and intensity. Frame averaging and smoothing are applied to reduce the salt and pepper noise signals, without any loss of infirmations, Babinsky and Edwards (1996), Farina et al. (1993) and Lee and Yianneskis (1993). A 3 x 3 spatial median filter was then used to remove any isolated pixels due to imperfections of the liquid crystal layer.

Image processing was done using MathCAD 2000. Image processing begins with importing hue-only images for the test plate which is 768×576 pixels and the hue-temperature calibration curve were used to covert each hue matrix values to temperature matrix. A code was written to calculate heat transfer coefficient and film cooling effectiveness from temperature matrix values.

3.4.3 Calibration

The liquid crystal calibration was conducted on the actual test surface, in absence of of the cross flow and film cooling injection. The lighting and camera settings are identical to the actual experiments. A small increase in electrical power was applied to the constant heat flux surface until the entire spectrum of colour was displayed. When the temperature exceed the limit, liquid crystal cease to reflecting colour and become transparent. For each given settings of electrical power input to the test plate, 25 images were captured at a frame rate of 25 frames per second, at same time corresponding temperatures from the 10 thermocouples with known location were recorded by data acquisition modules. RGB images are then transformed into Hue-only image. The hue-temperature calibration curve used in the present study is shown in Fig. 3.8. For the temperature and hue calibration, two different sets of calibration were conducted, the first calibration before the experiment and one after the experiment. These two different sets of data points collapsed on to the same calibration curve and did not show any shift in calibration.

A 5th order polynomial was generated which gave the best fit through calibration data points. The R^2 of curve fit, defined Eqn. 3.4 was calculated to be 0.998.

$$R^2 = 1 - \frac{SSE}{SST} \tag{3.4}$$

where SSE and SST is defined as

$$SSE = \sum (T_i - \hat{T}_i)^2 \tag{3.5}$$

$$SST = \sum (T_i^2) - \frac{\sum (T_i^2)}{n} \tag{3.6}$$

where T_i is the measured temperature and $\hat{T}_i$ is the mean temperature.

3.4.4 Test Procedure

The primary flow in the wind tunnel, the secondary flow though the injection tubes and the heat flux from the test surface can be changed to conduct the experiments under different conditions.

Heat transfer coefficients can be determined in two different ways. Fist method is operating experimental set up with heated injection with a given heat flux value. The heat transfer coefficient is defined using the difference between the heated wall temperature and the adiabatic wall temperature that was measured under identical flow conditions.

The second method of calculating heat transfer coefficient is to operate the tunnel with unheated injection with a given heat flux value. In this case, the temperature of primary flow has to be equal to the temperature of the secondary flow. The heat transfer coefficient is defined using the difference between the heated wall temperature and the free stream recovery temperature and in this case the adiabatic wall temperature and free stream recovery temperature are the same for unheated injection.

Adiabatic wall temperatures are determined by operating the set up with injection of the heated secondary air and no heat flux from the test surface.

In all cases, the primary flow, the secondary flow and the wall heat flux are set for a given operating conditions and run for an half hour in order for the experimental set up to come to a steady-state. Small adjustments in the primary flow rate, secondary flow rate or wall heat flux are made during the test when necessary to maintain the desired M, U_∞ and q'' values.

Velocity and temperature profiles at the outlet of the injection slots in the absence of primary flow are measured with hot wire system and thermocouples. The secondary air temperature, T_2, is taken as measured by a thermocouple located blow injection hole. The difference between this measured temperature varies by less than $\pm 2\%$ along the injection holes and velocity profile variation is $\pm 5\%$.

3.5 Uncertainty Analysis

Uncertainties are evaluated by the method of Kline and McClintock (1953). Corrections for radiation form the heated test surface with liquid crystal and conduction in the constant heat flux composite are included in the analysis. The uncertainty in heat transfer coefficient, h was $\pm 4.5\%$ in the near hole regions and decreased to $\pm 2.5\%$ far down stream. The typical uncertainty in effectiveness was about $\pm 5\%$ in the near hole, and increased to $\pm 15\%$ far downstream. The further details of uncertainty analysis are described in Appendix.

Re_m	DR	VR	M	I
15,000	1	0.3	0.3	0.09
15,000	1	0.5	0.5	0.25
15,000	1	0.9	0.9	0.81
15,000	1	1.2	1.2	1.44
30,000	1	0.1	0.1	0.01
30,000	1	0.3	0.3	0.09
30,000	1	0.5	0.5	0.25
30,000	1	0.9	0.9	0.81
45,000	1	0.1	0.1	0.01
45,000	1	0.3	0.3	0.09
45,000	1	0.5	0.5	0.25

Table 3.1: Test matrix for the heat transfer coefficient

Re_m	DR	VR	M	I
15,000	0.92	0.3	0.276	0.0828
15,000	0.92	0.5	0.46	0.23
15,000	0.92	0.9	0.828	0.7452
15,000	0.92	1.2	1.04	1.248
30,000	0.92	0.1	0.092	0.0092
30,000	0.92	0.3	0.276	0.0828
30,000	0.92	0.5	0.46	0.23
30,000	0.92	0.9	0.828	0.7452
45,000	0.92	0.1	0.092	0.0092
45,000	0.92	0.3	0.276	0.0828
45,000	0.92	0.5	0.46	0.23

Table 3.2: Test matrix for the film cooling effectiveness

Position	Martials	Purpose
Top	Stainless steel foil	Convective heat transfer surface
	Silicon impregnated sheet	Thermal Conductance, Electrical insulation
	Inconel	Heating element
	Tufnol	Thermal insulation
	Styrofoam	Thermal insulation
Bottom	Mild Steel	Mechanical support

Table 3.3: Composition of the constant heat flux test plate

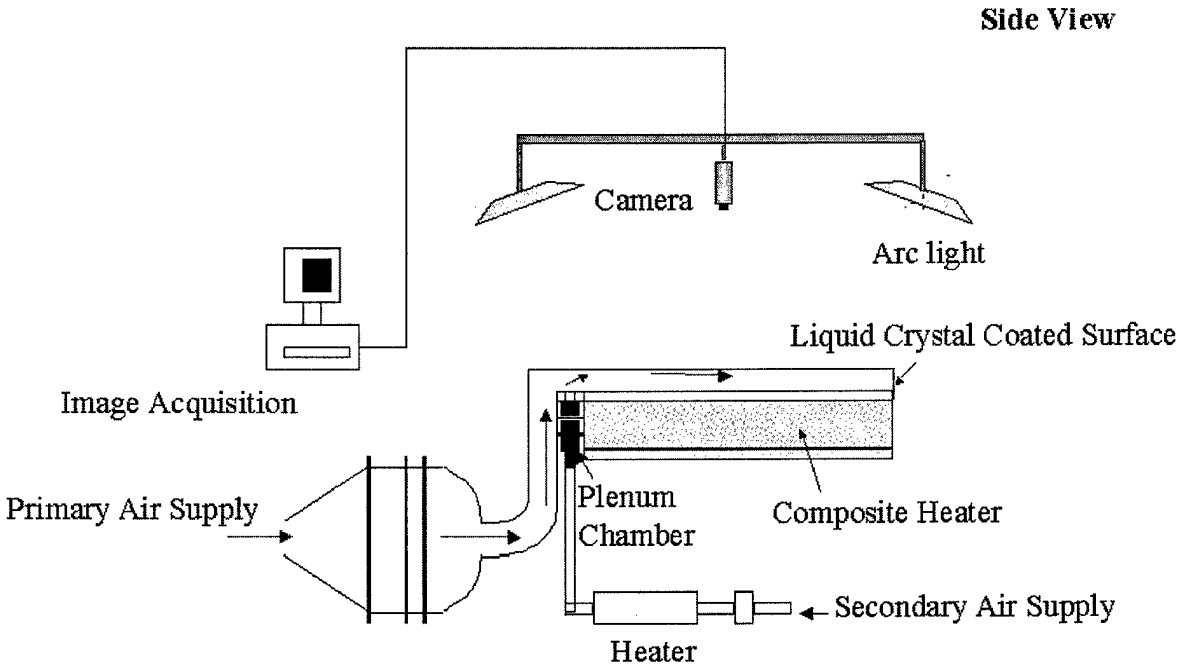

Figure 3.1: Experimental set-up

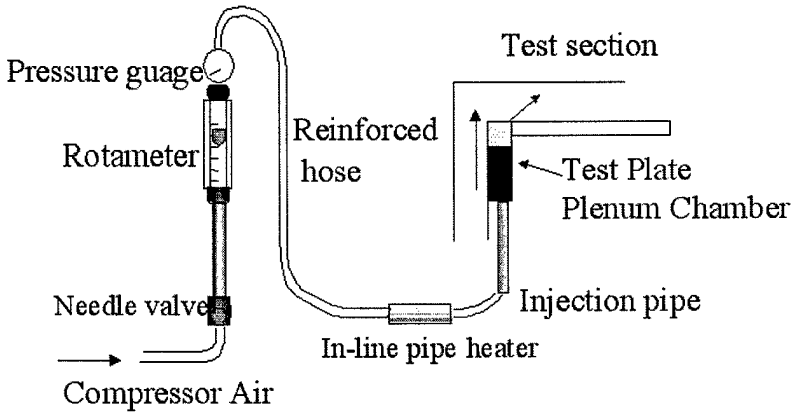

Figure 3.2: Flow circuit for Secondary Injection

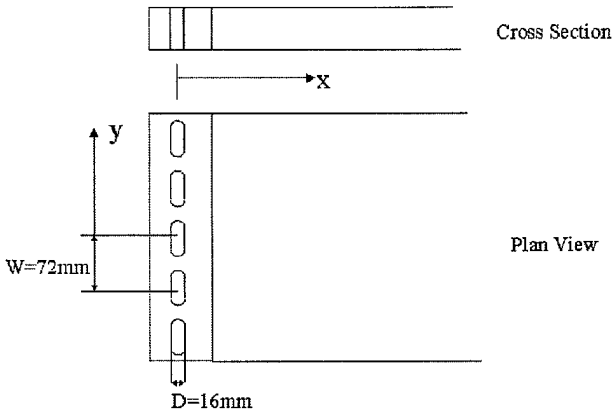

Figure 3.3: Hole Geometry

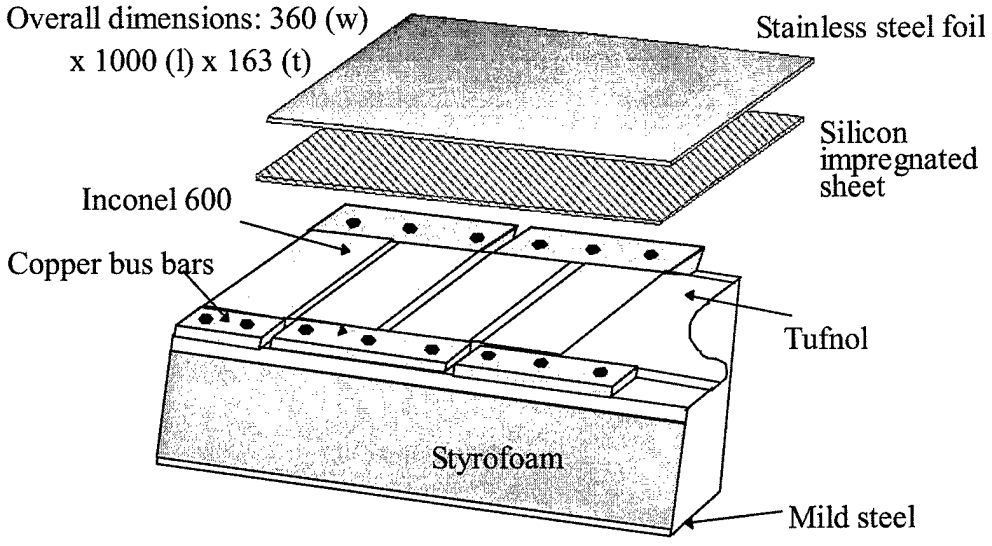

Figure 3.4: Test plate with a constant heat flux

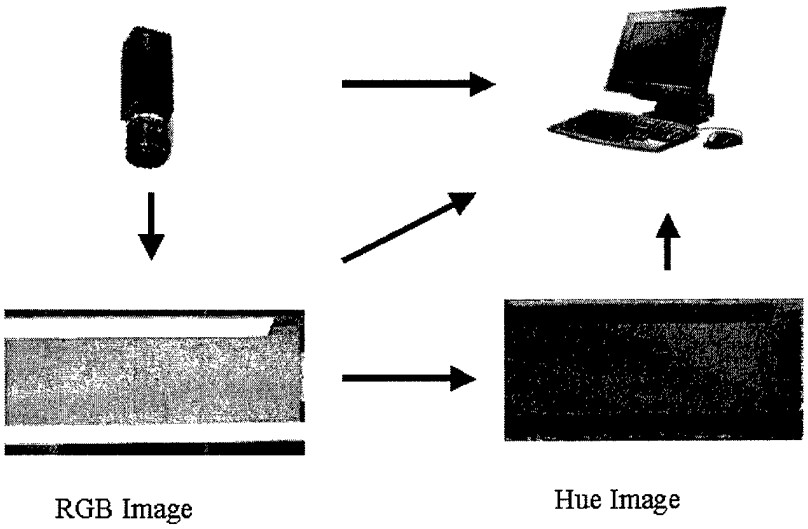

Figure 3.5: Image acquisition and processing

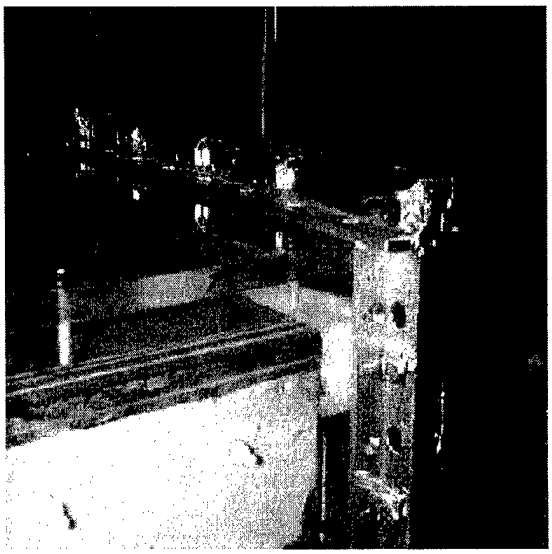

Figure 3.6: Photograph of test rig 1

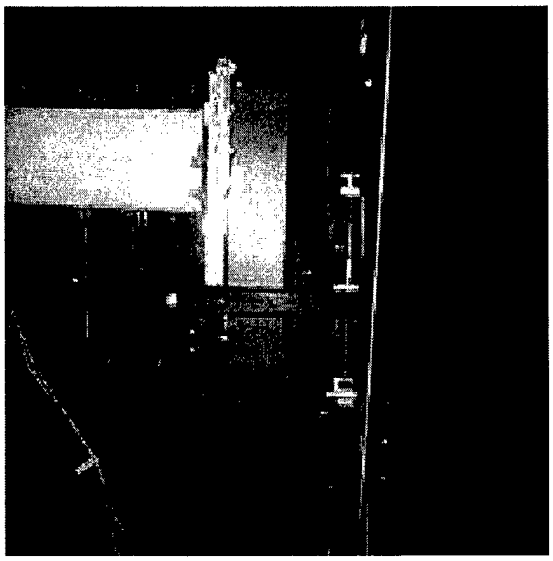

Figure 3.7: Photograph of test rig 2

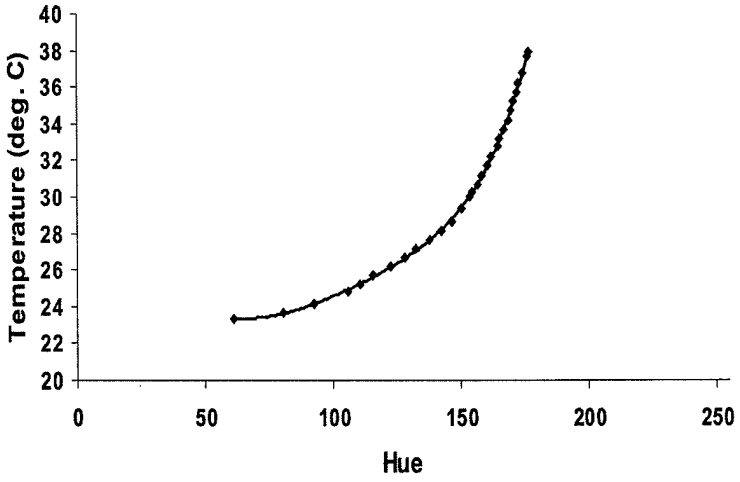

Figure 3.8: Calibration

Chapter 4

Results and Discussion

4.1 Introduction

The results and discussion sections are divided into two parts, the first section of the film cooling effectiveness and latter section of the heat transfer coefficient measurement.

The pressure difference of the suction side of the turbine blade and pressure side drives a sink-like flow characteristics near the tip of the pressure side of the turbine blade give rise to high velocities and accelerations into the tip clearance gap. The turbine blade generally has a sharp corner at the entrance of the gap which induces a separation bubble formation at the pressure side corner of the in the clearance gap. The presence of a separation bubble on the blade tip was examined by Bindon (1986) and Sjolander and Cao (1995). Heyes et al. (1993) also examined the effect of the corner radius in a linear cascade model and showed that the corner radius had a significant effect on formation and sizes of the separation bubble. The separation bubble in the clearance gap also contributes to reducing clearance gap mass flow rate, hence reducing tip leakage losses.

Reynolds number and blowing ratio are based on the clearance gap hydraulic diameter for the main flow. Measurement from the central section of the test plate ($z/W = 0 \sim 1$) is used to obtain the laterally-averaged values, in order to minimize test channel side-wall effects.

4.2 Film Cooling Effectiveness Measurements

Effect of Blowing Ratio on Effectiveness

Fig. 4.1 illustrates the effects of increasing blowing ratio on the laterally-averaged effectiveness values with Re_m=30,000. These display are an expected tendency based on previous results on a flat plate injection by Yuen (2000); the film cooling effectiveness varies from near unity value at the point of injection to zero far downstream, where the secondary flow dilute and the adiabatic wall temperature approaches the free stream values.

In the case of a flat plate film cooling, there is an optimum blowing ratio due to the fact that there is lift-off of coolant from boundary layer around M=0.4~0.6. In the case of clearance gap cooling, the geometrical restriction constrain the early development of lift-off as the flow is not freely allowed to expand into the free stream, hence no optimum is found.

The laterally-averaged effectiveness increase monotonically with increasing blowing ratio up to M=0.5 and reaches near maximum profile at this point. Further increase in blowing ratio does not significantly increase the effectiveness and stay at almost same level as M=0.5 case. However, in the case of the highest blowing ratio of M=0.9, there is apparent lift off of coolant taking place at the clearance gap. Slightly lower effectiveness values compared to M=0.5 case are measured in the near hole region up to x/D=4. After subsequent reattachment of coolant at downstream region, slightly higher effectiveness values are shown than in the M=0.5 case. These blow off effect are far more profound in the case of flat plate cooling geometry.

Effect of Re number on Effectiveness

The boundary layer thickness depends on the Reynolds number increases. In a flat plate film cooling geometry, Liess (1975) suggested that in the case of smaller boundary layer at the point of injection, the coolant experience higher fluid momentum close to the wall than in the case of a thicker boundary layer. This results in effectiveness increase since the coolant remain closer to the wall. Goldstein et al. (1968) found that doubling the displacement thickness of the freestream boundary layer have reduced effectiveness by 30%.

Fig. 4.2 shows a set of results to illustrate the relative independence of the laterally-averaged effectiveness values with changes in Reynolds number, a small decrease as

Reynolds number can be seen. The boundary layer development in the blade tip cooling geometry is different from the flat plate cooling geometry and fluid dynamic measurement of the flow is required for further insight of the effect of Reynolds number in the tip cooling geometry.

Spanwise Variation of Effectiveness

Fig. 4.3 and Fig. 4.4 show the colour contour plot of variations in the film cooling effectiveness, note the good symmetry in the results. At the streamwise location closest to film cooling injection, effectiveness values of near unity are recorded, in the case of the higher coolant blowing ratio of M=0.5 and above cases, Fig. 4.3(B), Fig. 4.3(C), and Fig. 4.3(D).

The discrete location of injection holes are clearly shown in the data. The effectiveness values are higher at the centre of hole and drop considerably in between injection holes. However, the minimum η value of around 0.4 are still provided even at the mid-point between the injection holes (z/W=-1/5,-0.5,0.5,1.5) at higher blowing ratio of M=0.5 and above. In the current set-up, the close spanwise spacing of the holes prevents any zero effectiveness regions between the holes ensuring a good coverage of film cooling flow. The spanwise variations in effectiveness is used to establish magnitude of local blade tip temperature gradients hence the size of the thermal stresses.

In Fig. 4.3 and Fig. 4.4 between z/W of 0 and -1 shows non-uniform result profile. This is caused by accidental contamination of liquid crystal with plaster coupled with the scratch on the perspex case which effects local temperature measurement. This problem can be solved with new batch of liquid crystal and construction of new scratch free perspex casing.

Spanwise variations of effectiveness tends to be highest at the highest blowing ratio. All the effectiveness measured decrease monotonically in the downstream direction. In summary, the results shows that the spanwise variations are small for small blowing ratio but increases with higher blowing ratio.

4.3 Heat Transfer Coefficient Measurements

Effect of Blowing Ratio on Nusselt number

Fig. 4.5 displays the measured effect of increasing blowing ratio on the laterally-averaged Nusselt numbers for the case of Re_m=45,000. The laterally-averaged heat transfer coefficient, presented here in Nusselt number form, display a classical sharp-edge channel entrance distribution with low values immediately downstream of the entrance (pressure side) corner attributed to flow separation. The values then rise rapidly in the streamwise direction, reaching a maximum around the value of x/D of 3.5, as the flow develops streamwise, Nusselt numbers then decreases slowly.

The film cooling injection produce the highest heat transfer coefficient immediately downstream of the injection holes. However, the surface is still cooled since the film cooling injectant is at a lower temperature than the mainstream. Temperature difference between surrounding fluid and the clearance gap are smaller then without film cooling.

The Nusselt number are much higher at the near holes and reaches close to 160 and drops to around 80 in the far downstream for M=0.9 case. In the lower blowing ratio, the Nusselt number profile is much more flatter at the maximum level of around 110 at x/D=3.5.

The effect of blowing ratio on Nusselt number in tip clearance is different from conventional film cooling geometry. The important effect in this case is the general tendency for a small increase in Nusselt number over nearly all of the protected surface with increasing in blowing ratio. At higher blowing ratio, more coolant is injected into the boundary layer which in turn act as bigger heat sink and also there is an increase in the free stream velocity due to film cooling injection. This effect is particulary the case in the narrow passage of the clearance gap, where the injection hole diameter is around 20% of the clearance gap height. This effect would be insignificant in wide passage, commonly used in film cooling studies.

This increase in the peak value near the injection hole due to injection provides an important parameter to predict the blade tip thermal loading. The temperature of film injection needs to be low enough to prevent increase in thermal loading on the tip due to injection, otherwise the high blowing ratio can lead to higher thermal loading on the tip which is an undesirable effect.

Effect of Re number on Nusselt number

Fig. 4.6 shows experimental results conducted in various film blowing ratios for all three values of Reynolds number used in this study. The Reynolds number has a significant effect on the laterally averaged Nusselt number and results indicate that the higher Reynolds number, the Nusselt number are higher. The increase in Reynolds number effectively means increase in the amount of tip leakage flow, leading to an increase in the flow local velocity, as a consequence the local Nusselt number is expected rise. It is worth noting that generally an increase in tip leakage flow has detrimental effect on aerodynamic performance and as we can see here, it also has a relative effect on the heat transfer levels.

Spanwise Variation of Heat Transfer Coefficient

The heat transfer coefficient is evaluated from changes in the adiabatic temperature and wall temperature at a given heat flux (Eqn. 2.3). Both the adiabatic temperature and wall temperature with heat flux have a similar spanwise profile, meaning that the overall variation of h across the test span is small when compared to the variation of the effectiveness.

Fig. 4.7 and Fig. 4.8 shows variations of convection coefficients along the spanwise direction. The local variation for M=0.1 are very small, the order of around ± 5 percent while the variation for M=0.9 range is around ± 15 percent at the streamwise location closest to the holes but decreases rapidly in the downstream.

The small spanwise variation support the idea that the heat transfer coefficients are dominated by the channel entrance effect at lower blowing ratio, and are only elevated significantly by injection at the higher values.

4.4 Comparison with computational data

Fig. 4.9 shows the comparison between a current set of results, an experimental value of Kim and Metzger (1995) and a computational work of Ameri and Rigby (1999). The overall agreement between current data and other results are quite good. This is particularly the case to the comparison with computational results which shows good agreement, a slight over-prediction near the hole injection up to 7.5 hole diameters distance to streamwise direction can be seen. The predictions for the laterally-averaged effectiveness values

further downstream of the injection are very similar to each other in all three test cases. The deviation between computed and experiential profiles of the laterally-averaged effectiveness are within the uncertainty of the current experimental data and further detailed analysis on the uncertainty are discussed in Appendix.

Fig. 4.10 compares the current experimental data, the computed laterally-averaged Nusselt number of Ameri and Rigby (1999) and the experimental values of Kim and Metzger (1995).

The agreement with Kim and Metzger's experimental data was very good except near the hole region. The agreement shows a distinct improvement away from the hole and difference between two experiential profiles of the laterally-averaged Nusselt number is within the uncertainty of the current experimental data except immediate vicinity of the injection hole region.

The computational calculation of Ameri and Rigby (1999) over-predicted the Nusselt number by around 20% at the position of X/D=3.5 downstream location where the peak in Nusselt number is found. After the peak value, the computational prediction improves slight. However position of the maximum is around same streamwise distance away from the hole as in the experiments. Overall computational prediction of the laterally-averaged effectiveness are significantly better than those of the laterally-averaged Nusselt number.

4.5 Conclusion

An experimental investigation of a turbine blade tip film cooling geometry were conducted. The effect of Reynolds number and blowing ratio are examined for an injection on the blade tip itself close to the pressure surface corner and presented in the earlier chapter.

The wide band liquid crystal thermography experimental technique is used. This technique is capable of achieving full coverage of the measurement of the surface temperature, from which the effectiveness and heat transfer coefficient measurements can be found with typical uncertainties of $\pm 4\%$ and $\pm 8\%$ respectively.

Film cooling injection with a single raw of elongated holes near the pressure side corner provide significant protection to the tip from the hot clearance gap leakage flow. It provides a blanket of coverage lasting far downstream of the holes in higher blowing ratio.

Injection generally increases the convection coefficients but also increase film cooling effectiveness. Injection induced elevation in heat transfer coefficient, if the film cooling

injection temperature is not sufficiently low relative to the clearance leakage flow, injection can lead to increase in thermal loading on the blade tip. The colour contour plot of film cooling effectiveness and heat transfer coefficient provide a clear graphical representation of a full coverage distribution for heat transfer studies.

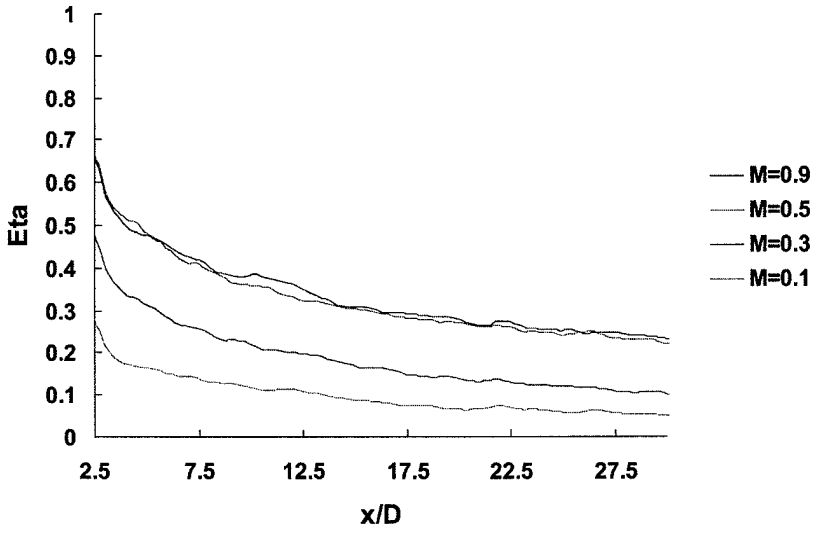

Figure 4.1: Effect of Blowing Ratio on Laterally Averaged Effectiveness Re=30,000

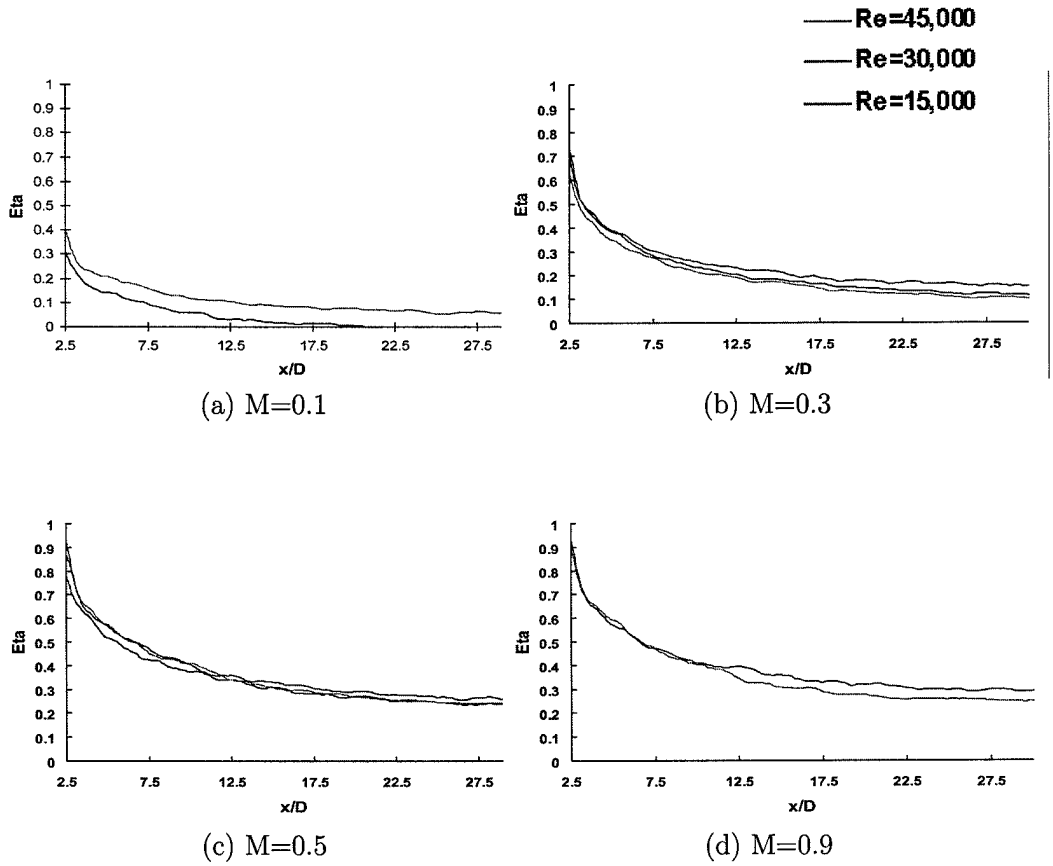

(a) M=0.1 (b) M=0.3

(c) M=0.5 (d) M=0.9

Figure 4.2: Effect of Re number on Laterally Averaged Effectiveness

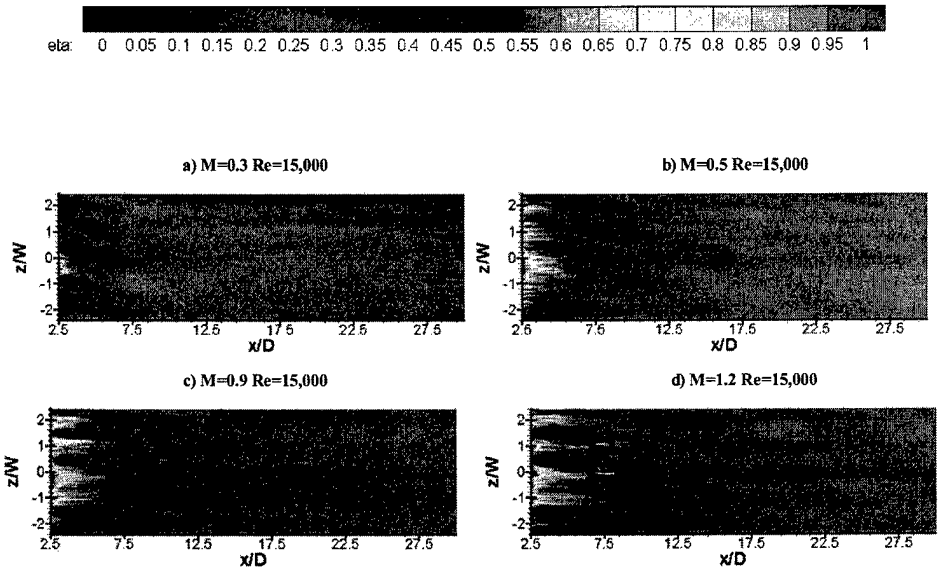

Figure 4.3: Film Cooling Effectiveness Re=15,000

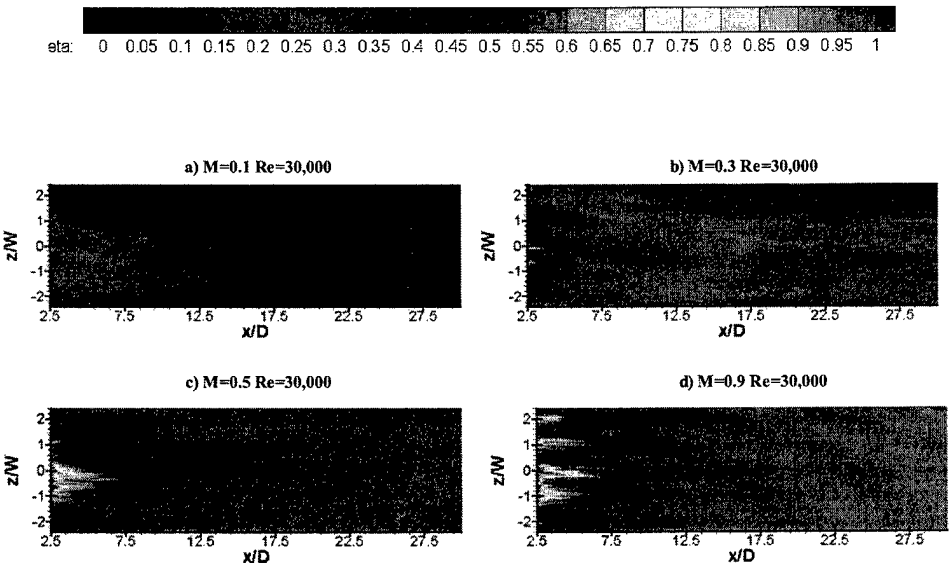

Figure 4.4: Film Cooling Effectiveness Re=30,000

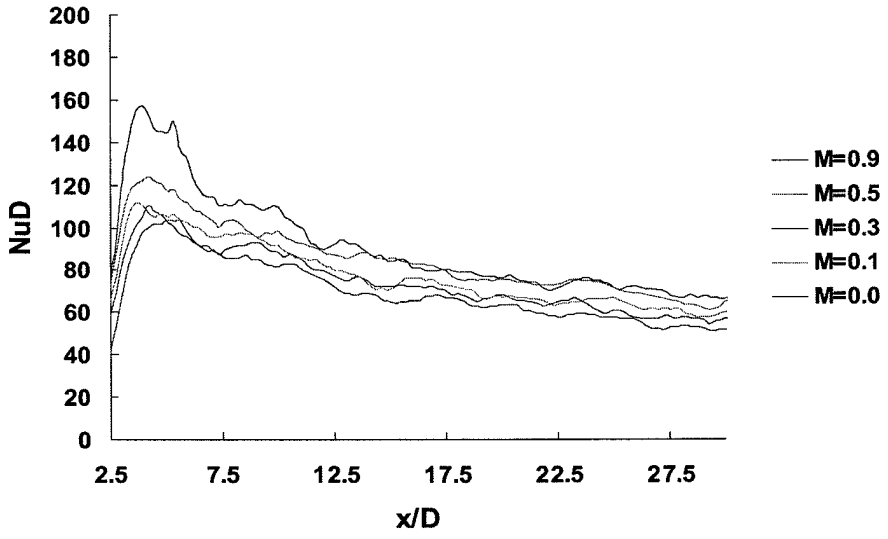

Figure 4.5: Effect of Blowing Ratio on Laterally Averaged Nusselt Number Re=30,000

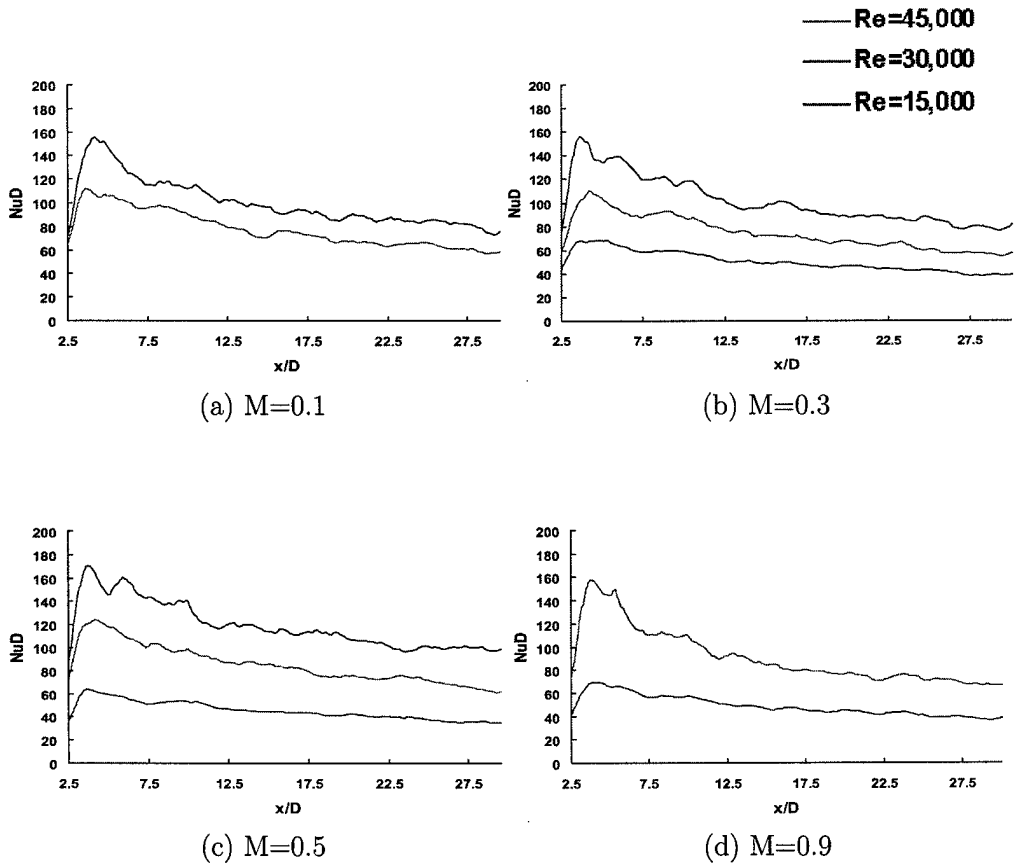

(a) M=0.1 (b) M=0.3

(c) M=0.5 (d) M=0.9

Figure 4.6: Effect of Re number on Nusselt Number

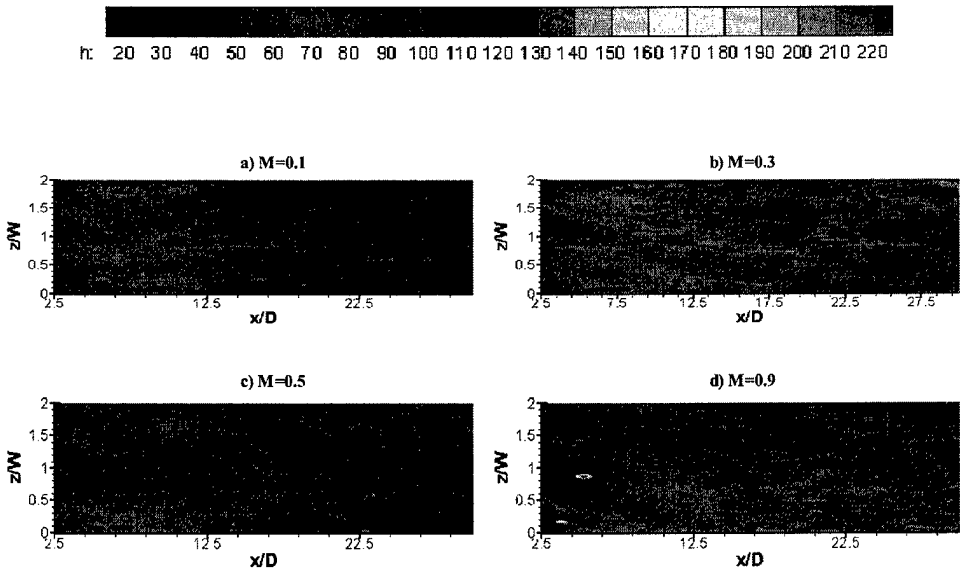

Figure 4.7: Heat Transfer Coefficient Re=30,000

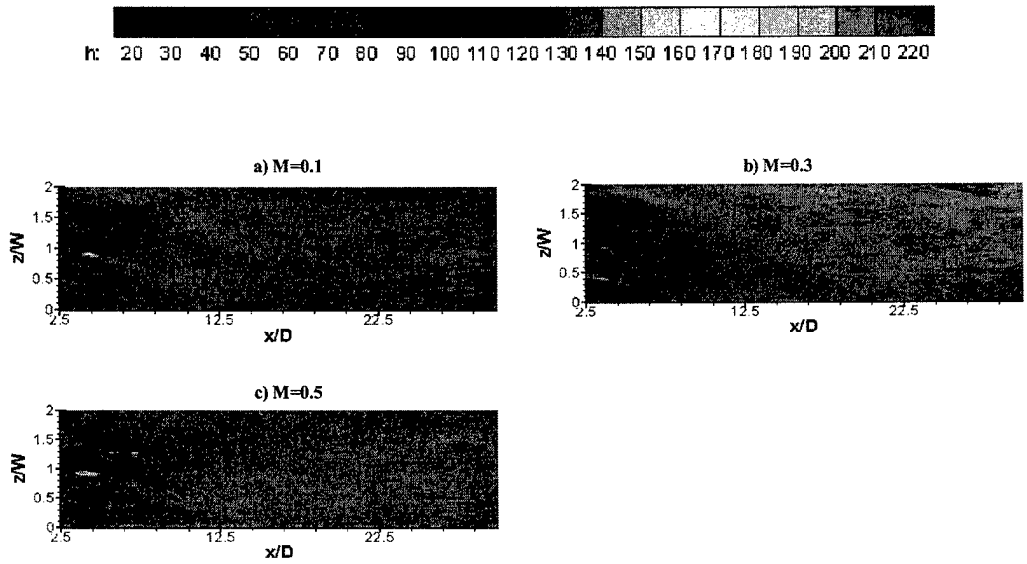

Figure 4.8: Heat Transfer Coefficient Re=45,000

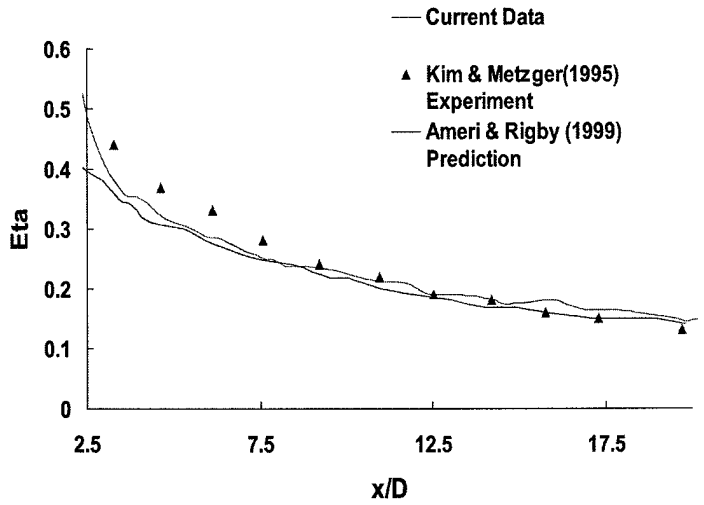

Figure 4.9: Laterally Averaged Effectiveness Re=45,000 M=0.3

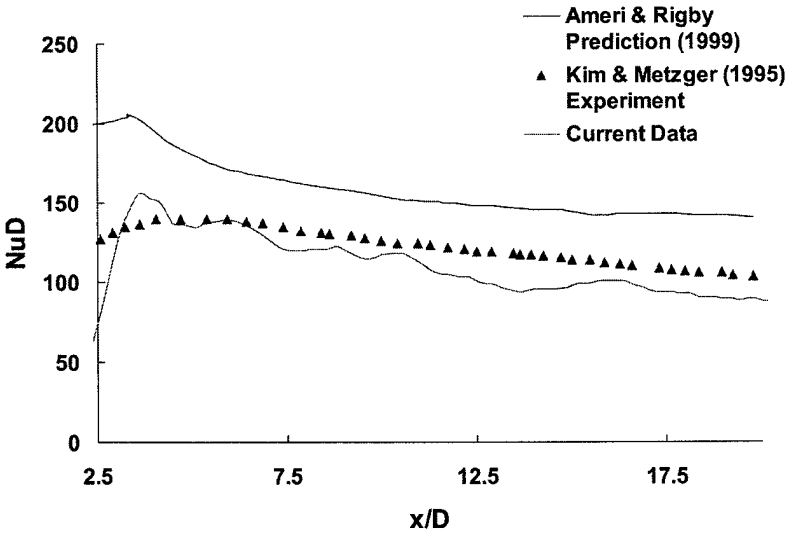

Figure 4.10: Laterally Averaged Nusselt No Re=45,000 M=0.3

Bibliography

Ameri, A.A., Rigby, D.L. (1999). Analysis of supersonic stall bending flutter in axial-flow compressor by actuator disk theory. Technical Paper 1999-209165, NASA. The 14th International Symposium on Air Breathing Engines, Florence, Italy.

Ammari, H.D. (1989). *The Heat Transfer Coefficient on Film Cooled Surfaces.* Ph. D. thesis, University of Nottingham.

Azad, G.S., Han, J.C., Teng, S., and Boyle, R.J. (2000). Heat transfer and pressure distributions on a gas tubribne blade tip. *ASME TURBOEXPO 2000 2000-GT-194.*

Babinsky, H., Edwards, J.A. (1996). Automatic liquid crystal thermography for transient heat transfer measurements in hypersonic flow. *Experiments in Fluids 21,* 227–236.

Bindon, J.P. (1986). Visualization of axial turbine tip clearance using a linear cascade. Cued/a-turbo tr122 whittle labratory, Cambridge University.

Booth, T.C., Dodge, P.R., Hepworth, H.K. (1982). Rotor-tip leakage:part1-basic methodogy. *ASME Journal of Engineering for power 104,* 154–161.

Camci, C., Kim, K., Hippensteele, S.A. (1992). A new hue capturing technique for the quantitative interpretaion of liquid crystal images used in convective heat transfer studies. *ASME Journal of Turbomachinery 114,* 765–775.

Chen, G., Dawes, W.N., Hodson, H.P. (1993). A numerical and experimental investigaion of turbine tip gap flow. *AIAA 93-2253.*

Chyu, M.K., Metzger, D.E., Hwan, C.L. (1987). Heat transfer in shrouded rectangular cavities. *Journal of Thermophysics and Heat Transfer 1,* 247–252.

Chyu, M.K., Moon, H.K., and Metzger, D.E. (1989). Heat transfer in the tip region of grooved turbine blades. *Journal of Turbomachinery 111,* 131–138.

Ekkad, S. V., Zapata, D. and Han, J. C. (1997). Heat transfer coefficients over a flat surface with air and co2 injection, through compound angle holes using transient

liquid crystal image method. *ASME Journal of Turbomachinery 119*, 580–586.

Eriksen, V.L. (1971). *Film Cooling Effectiveness and Heat Transfer with Injection Through Holes.* Ph. D. thesis, Universiy of Minnesota.

Farina, D.J., Hacker, J.M., Moffat, R.J., Eaton, J.K. (1993). Illuminant invariant calibration of thermochromic liquid crystals. *Visualisation of Heat Transfer Processes ASME 253*, 1–11.

Goldstein, R.J. (1971). Film cooling. *Advances in Heat Transfer 7*, 321–379.

Goldstein, R.J., Eckert, E.R.G. and Ramsey, J.W. (1968). Film cooling with injection through holes: Adiabatic wall temperatures downstream of a circular hole. *ASME Journal of Engineering for Power*, 384–395.

Goldstein, R.J., Yoshida, T. (1982). Boundary layer amd laminar injection on film cooling performance. *Journal of Heat Transfer 104*, 355–362.

Hennecke, D.K. (1984). *Heat Transfer Problems in Aero-engines.* Hemisphere Publications, Inc., Washington, DC USA.

Heyes, F.J.G., Hodson, H.P., and Dailey, G.M. (1993). Measurement and prediction of tip clearance on the tip leakage flow in axial turbine cascade. *ASME Journal of Turbomachinery 115*, 643–651.

Kim, Y.W., Downs, J.P., Soechting, F.O., Abdel-Messeh, W., Steuber, G.D., Tanrikut, S. (1995). A summary of the cooled turbine blade tip heat transfer and film effectiveness investigations. *ASME Journal of Turbomachinery 117*, 1–11.

Kim, Y.W., Metzger, D.E. (1995). Heat transfer and effectiveness on film cooled turbine blade tip models. *ASME Journal of Turbomachinery 117*, 12–21.

Kline, S.J., Mcklintock, F.A. (1953). Describing uncertainties in single sample experiments. *Mechanical Engineering January*, 3–8.

Lakshminarayana, B. (1970). Methods of predicting the tip clearance effects in axial flow turbomachinery. *Journal of Basic Engineering*, 467–82.

Lee, K.C., Yianneskis, M. (1993). An image processing technique for the analysis of thermotic distribution utilising liquid crystals. Imaging in Transport Processes.

Liess, C. (1975). Experimental investigation of film cooling with ejection from a row of holes from the application to gas turbine blades. *ASME Journal of Engineering for Power*, 21–27.

Martinez-Botas, R.F., Lock, G. D., Jones, T.V. (1995). Heat transfer measurments in an annular cascde of transonic gas turbine blades using the transient liquid crystal technique. *ASME Journal of Turbomachinery 117*, 425–431.

Mayle, R.E., Metzger, D.E. (1982). Heat transfer at the tip of an unshrouded turbine blade. Proc. 7th Intl. Heat Conf. Washington, D.C.

Metzger, D.E., Larson, D.E. (1986). Use of melting point surface coating for laocal convection heat transfer measurements in rectangular channels with 90-degree turns. *ASME Journal of Heat Transfer 108*, 48–54.

Metzger, D.E., Rued, K. (1989). The influence of turbine clearnce gap leakage on passage velocity and heat transfer near blade tips:part 1-sink flow effects on blade pressure side. *ASME Journal of Turbomachinery 1011*, 284–292.

Rastogi, A.K. (1972). *Effectivness and Heat Transfer of Three-Dimensional Film Cooling Slots.* Ph. D. thesis, Imperial College of Science, Technology and Medicine, London.

Sen, B., Schmidt, D.L. Bogard,D.G. (1996). Film cooling with compound angle holes:heat transfer. *ASME Journal of Turbomachinery 118*, 800–806.

Sjolander, S.A. and Cao, D. (1995). Meaurement of the flow in an idealized turbine tip gap. *ASME Journal of Turbomachinery 117*, 578–584.

Vedula, R. J. and Metzger, D. E. (1991). A method for the simultaneous determination of local effectiveness and heat transfer distribution in three temperature convetion situation. *ASME Paper No.91-GT-345*.

Yuen, C.H.N. (2000). *Measurement of Local Heat Transfer Coefficient and Film Cooling Effectiveness in Film Cooling Geometries.* Ph. D. thesis, Imperial College of Science, Technology and Medicine, London.

Appendix A

Appendix

A.1 Uncertainty Analysis

Uncertainties of the effectiveness and the heat transfer coefficient were evaluated according to the method of Kline and McClintock (1953) and Ericksen (1971). The uncertainty in the heat transfer coefficient is given by equation A.1, and the effectiveness uncertainty equation is shown in equation A.12. The local heat flux, q'', was derived from the electrical power input to the heat flux composite, and the temperatures T_w and T_{aw} were measured from the calibrated thermographic liquid crystals.

$$\frac{\partial h}{h} = \left[\left(\frac{\delta q''}{q''} \right)^2 + \left(\frac{\delta T_w}{T_w - T_{aw}} \right)^2 + \left(\frac{\delta T_{aw}}{T_w - T_{aw}} \right)^2 \right]^{\frac{1}{2}} \tag{A.1}$$

A.1.1 $\left(\frac{\delta q''}{q''}\right)^2$ term

Corrections for radiation from the heated test surface and conduction out the back of the test surface were included in the analysis, such that the subtraction of these corrections from the average heat flux gave the net local heat flux, equation A.2. Equation A.3 defines the corresponding uncertainty value.

$$q'' = q''_g - q''_r - q''_{bc} \tag{A.2}$$

$$\frac{\partial q''}{q''} = \left[\left(\frac{\delta q_g''}{q_g''} \right)^2 + \left(\frac{\delta q_r''}{q_r''} \right)^2 + \left(\frac{\delta q_{bc}''}{q_{bc}''} \right)^2 \right]^{\frac{1}{2}} \tag{A.3}$$

where q'' is the wall heat flux, q_g'' is the heat flux generated from the heater, q_r'' is the heat flux radiation correction loss, and q_{bc}'' represents the heat flux correction for conduction loss at the back of the heated test plate.

The heat generation term was calculated from electrical current, i, and voltage, v, supplied to the heater, equation A.4, where A is the heated area, and the associated uncertainty in q_g'' is defined in equation A.5.

$$\partial q'' = \frac{vi}{A} \tag{A.4}$$

$$\frac{\partial q_g''}{q_g''} = \left[\left(\frac{\delta v}{v} \right)^2 + \left(\frac{\delta i}{i} \right)^2 + \left(\frac{\delta A}{A} \right)^2 \right]^{\frac{1}{2}} \tag{A.5}$$

The uncertainties in the current and voltage were ± 0.05 ampere and ± 0.01 volt respectively. The measured area was accurate to $\pm 1mm^2$, which led to an accuracy of $\pm 2\%$ in heat flux.

The radiation loss term is expressed as equation A.6. The emissivity(ϵ) of the liquid crystal coating is assumed to be 0.96, and the Stefan-Boltzmann constant(σ) is given as $5.67 \times 10^{-8} W/m^2 K^4$.

$$q_r'' = \epsilon \sigma (T_w^4 - T_\infty^4) \tag{A.6}$$

The conduction loss from the heated plate was assumed on the one-dimensional heat flow through constant heat flux composite in equation A.7, where ΔT is the local temperature difference and A is the heated test surface.

$$q_{bc}'' = S \triangle T \tag{A.7}$$

$$S = \frac{1}{R_t A} = \frac{1}{[(1/h_\infty) + (L_1/k_1) + (L_2/k_2) + ...(L_n/k_n) + (1/h_{b\infty})]} \tag{A.8}$$

where R_t is the sum of all thermal resistance, h_∞ and $h_{b\infty}$ are the freestream transfer coefficients above and below the heated plate, L_n and k_n are the thickness and the corresponding thermal conductivity of each layer in the test plate.

The local value q'' was adjusted with the radiation and conduction losses from above equation, and the combined uncertainties gave a maximum total uncertainty of less than 1.5% in $\delta q/q$ term.

A.1.2 $\left(\frac{\delta T_w}{T_w - T_{aw}}\right)^2 + \left(\frac{\delta T_{aw}}{T_w - T_{aw}}\right)^2$ terms

Corrections were applied to the measured wall temperature to take the heat loss through thermocouple leads, $\triangle T_{lw}$, in the liquid crystals calibration procedure. Equation A.9 shows the corrected wall temperature.

$$T_w = T_{TLC} + \triangle T_{lw} \tag{A.9}$$

A.1.3 Lateral conduction error

The local wall temperature is influenced by the heat flux distribution within the wall at high temperature gradient, for example, near the point of injection. If it is assumed that there is no temperature change in the Y direction within the test surface, an energy balance on the element can be expressed as following equations for the temperature error due to heat conduction within the test surface.

$$\triangle(T_w - T_\infty) = -\frac{kb}{hD^2}\left[\frac{\partial^2(T_w - T_\infty)}{\partial(x/D)^2} + \frac{\partial^2(T_w - T_\infty)}{\partial(z/D)^2}\right] \tag{A.10}$$

$$\triangle\eta_{wc} = -\frac{kb}{hD^2}\left[\frac{\partial^2(\eta)}{\partial(x/D)^2} + \frac{\partial^2(\eta)}{\partial(z/D)^2}\right] \tag{A.11}$$

where thickness of the test surface is b, h is the heat transfer coefficient on the test surface, D is the diameter of the injection hole, k denotes the equivalent thermal conductivity for the wall.

A.1.4 The combined uncertainty

The uncertainty in heat transfer coefficient, h, was 4.5% in the near hole regions and decreased to 2.5% far downstream. The uncertainty is depend on blowing ration. The uncertainty at larger blowing ratios was greater than that at small blowing ratios, because the temperature difference, $T_w - T_{aw}$, in equation A.1, decreased for the same δT_w or δT_{aw} with increasing blowing ratio.

The approach of uncertainty analysis for film cooling effectiveness was very similar to that for the heat transfer coefficient described. The uncertainty in the film cooling effectiveness. is given in equation A.12

$$\frac{\partial \eta}{\eta} = \left[\left(\frac{\delta T_{aw}}{T_{aw} - T_\infty} \right)^2 + \left(\frac{\delta T_2}{T_2 - T_\infty} \right)^2 + \left(\frac{\delta T_\infty}{T_2 - T_\infty} \right)^2 \left(1 - \frac{1}{\eta} \right)^2 \right]^{\frac{1}{2}} \tag{A.12}$$

The typical uncertainty in effectiveness was about 5% in the near injection hole, and increased to 15% at downstream locations.